

Contents lists available at ScienceDirect

Materials Today Physics

journal homepage: https://www.journals.elsevier.com/ materials-today-physics



Thermal studies of nanoporous thin films with added periodic nanopores—a new approach to evaluate the importance of phononic effects



Y. Xiao, D. Xu, F.J. Medina, S. Wang, Q. Hao*

Department of Aerospace & Mechanical Engineering, University of Arizona, 1130 N Mountain Ave, Tucson, AZ, 85721, USA

ARTICLE INFO

Article history:
Received 27 November 2019
Received in revised form
7 January 2020
Accepted 12 January 2020
Available online 24 January 2020

Keywords: Phononic crystal Coherent/incoherent phonon transport Phonon size effect Phonon Monte Carlo simulation

ABSTRACT

Phonon transport within periodic nanoporous materials has been intensively studied for its potential applications in thermoelectrics, heat waveguides, thermal diodes, and heat imaging. It is now acknowledged that wave effects of lattice vibrations, i.e., phononic effects, are only important for ultrafine nanoporous structures and/or at cryogenic temperatures. Experimental evidence is usually found by comparing the thermal conductivities of periodic and aperiodic nanoporous Si films, or by measuring the specific heat to check the phonon dispersion variation. In this work, a new approach is used to evaluate the impact of possible wave effects, simply by comparing the thermal conductivity of the same Si thin film with increased rows of nanopores as drilled with a focused ion beam. In the temperature range of 85-300 K, it is found that the total thermal resistance of the thin film increases almost linearly with the number of rows, indicating dominant incoherent phonon transport or negligible wave effects. For nanopores with small spacing, the amorphous regions around pore edges can largely overlap so that the whole region can be treated as a homogeneous amorphous material with nanoporosity. When the pore spacing is larger, the amorphous pore edges expand the effective pore diameter that is used in the data analysis based on frequency-dependent phonon Monte Carlo simulations. A better understanding of these nanoporous films can benefit their applications in thermoelectrics and thermal management of thin-film-based electronic devices.

© 2020 Elsevier Ltd. All rights reserved.

1. Introduction

In recent years, nanoporous thin films have been widely studied for their potential applications in thermoelectrics [1–4], heat guiding, heat focusing [5], and thermal cloaking [6,7]. For a solid thin film, phonons can be diffusively scattered by the top and bottom film surfaces, resulting in a shorter phonon mean free path (MFP) Λ_{film} , comparing with the bulk phonon MFP Λ_{bulk} . Such classical phonon size effects lead to a reduced lattice thermal conductivity k_L from the bulk material [3]. Correspondingly, the thermal conductivity $k = k_E + k_L$ is reduced, where k_E is the electronic contribution to the heat conduction. A further k_L reduction can be achieved by drilling arrays of nanopores or other nanoporous patterns across a thin film.

Despite numerous measurements, there have been debates on the exact mechanisms of the observed k_L reduction within these nanoporous thin films. In earlier studies, phonon wave effects within a periodic nanoporous film were suggested to modify the phonon dispersion and thus dramatically decrease the k_L [1,8–12]. Along this line, nanoporous thin films were often referred to as "phononic crystals," in analogy to photonic crystals with periodic cavities to tailor optical properties [13,14]. However, the short phonon wavelengths at room temperature (e.g., 1–10 nm for bulk Si [15,16]) are still smaller than the fabricated nanoporous patterns with a pitch of at least 34 nm. The impacted phonon modes are mostly restricted to hypersonic modes with frequencies of ~100 GHz or less, instead of THz for majority of phonons carrying the heat [2,17,18]. In addition, the roughness of usually amorphous and/or oxidized pore edges can often be large compared to phonon wavelengths. High-resolution transmission electron microscopy (TEM) studies show a 1–2 nm native oxide surface layer around a nanopore with ~20 nm diameters [19]. Such a rough pore edge can diffusively scatter phonons and thus destroy the phonon phase

^{*} Corresponding author. E-mail address: qinghao@email.arizona.edu (Q. Hao).

coherence required for wave effects. Considering relatively large periodic patterns and the pore-edge diffusive phonon scattering, now it is widely acknowledged that incoherent phonon transport should be dominant for the measured k_L reduction at 300 K or above. In data analysis, an effective pore diameter due to pore-edge defects can often be used to match the theoretical predictions with the experimental results [20,21].

Only considering classical phonon size effects, temperature-dependent k_L for nanoporous Si has also been modeled for a bulk—nanoporous silicon device that can be used as a thermal rectifier [22,23]. An extended analytical model is also available for thin nanocomposite films, where the nanocomposite is made of a homogeneous matrix with dispersed nanoparticles [24]. In this aspect, a nanoporous thin film can be viewed as a nanocomposite film embedded with zero-thermal-conductivity nanoparticles. In another analytical model, the surface relaxation and elastic interaction among nanopores are further considered for their impact on the phonon dispersion [25].

Experimentally, coherent and incoherent phonon transport can be justified by comparing the thermal conductivities of periodic and aperiodic nanoporous thin films [5,26]. In principle, the nanopore displacement can largely weaken the wave effects that require a periodic structure for wave interference. On the other hand, incoherent phonon transport with diffusive pore-edge phonon scattering should yield the same k_L because the radiative mean beam length (MBL) remains the same for periodic and aperiodic patterns [2,27,28]. As the characteristic length of the nanoporous structure to modify the phonon mean free paths (MFPs), this MBL is proportional to the volume of the solid part divided by the pore surface area [29]. In experiments, such comparison between periodic and aperiodic patterns suggested phononic effects below 10-14 K for samples with >100 nm pitches [5,26]. The increased importance of phononic effects at such a low absolute temperature T is mainly due to the increased dominant phonon wavelength that is inversely proportional to T [30]. As a different approach, the existence of the phononic effect and its associated phonon dispersion variation can be justified by specific heat measurements of a nanoporous Si thin film, where no remarkable phononic effects were found above 77 K for Si films with pitches on the order of 100 nm [21]. With advanced techniques such as Brillouin light scattering, the phonon dispersion of nanoporous Si thin films was directly measured for phononic studies [31].

In this work, a new approach is proposed to evaluate the impact of possible phononic effects within periodic nanoporous thin films or more general two-dimensional (2D) nanoporous patterns, such as graphene with periodic pores as "antidots." [32,33] This approach is inspired by previous studies on photon transmission across a Bragg reflector with an increased number of periodic alternating layers [34]. Based on wave optics, the transmittance should decrease to a constant value over a certain number of periods, whereas the ray-tracing technique (i.e., particle view) predicts a continuously reduced photon transmittance due to added interfacial photon scattering. A similar case can be found for the cross-plane thermal resistance of a GaAs/AlAs superlattice, where the cross-plane thermal conductivity linearly increases with the increased number of periods (i.e., a constant cross-plane thermal resistance) with dominant coherent phonon transport [35]. These coherent phonons view the whole superlattice as a homogeneous medium and their MFPs are restricted by the total film thickness t, leading to a cross-plane $k_L \propto t$ and thus a constant cross-plane thermal resistance t/k_L per unit area. For periodic nanoporous thin films, the periodic layers within a Bragg reflector or superlattice are replaced by periodic nanopores. Following these two earlier studies, the same suspended 70-nm-thick and 10- μ m-long Si film was repeatedly measured for its in-plane thermal resistance R_{Si} , with added rows of 70-nm-diameter nanopores drilled with a focused ion beam (FIB). If strong coherent phonon transport existed, the expanded nanoporous region should yield an almost constant thermal resistance. In contrast, strong incoherent phonon transport should lead to linearly increased R_{Si} with an increased row number of nanopores, which is due to the increased phonon boundary scattering by pore edges within the volume, i.e., a reduced MBL. In experiments, two representative nanoporous thin films both yielded R_{Si} increased almost linearly with the number of rows, indicating strong incoherent phonon transport. Our conclusion was consistent with a recent study [26] but contradicted with one previous study using FIB-drilled Si thin films [11], the latter of which suggested strong phononic effects could exist at room temperature. The proposed approach can be generally applied to other periodic nanoporous thin films or 2D materials to evaluate the significance of coherent phonon transport.

2. Materials and methods

2.1. Device nanofabrication and thermal measurements

A T-junction microdevice was used for the proposed in-plane thermal measurements, with the short beam as the measured sample. Fig. 1a shows a scanning electron microscopy (SEM) image of the T-junction device. This microdevice was fabricated from the device layer of a commercial silicon-on-insulator wafer with FIB patterning followed by hydrofluoric acid etching to suspend the device. For electrical insulation, a $\mathrm{SiN_x}$ layer was coated on top of the Si layer with low-pressure chemical vapor deposition (LPCVD). The thickness of this $\mathrm{SiN_x}$ layer was 34 ± 0.5 nm, as measured with an optical thin film analyzer (Filmetrics F20). Along the long beam, a 10-nm-thick Cr adhesion layer and then a 100-nm-thick Au layer were deposited as a metal line to be used as a heater and electrical resistance thermometer in thermal measurements (highlighted in red in Fig. 1a). The metal-line width was ~2 μ m. The long beam was ~150 μ m long and ~2.5 μ m wide. The short beam was ~9.96 μ m long

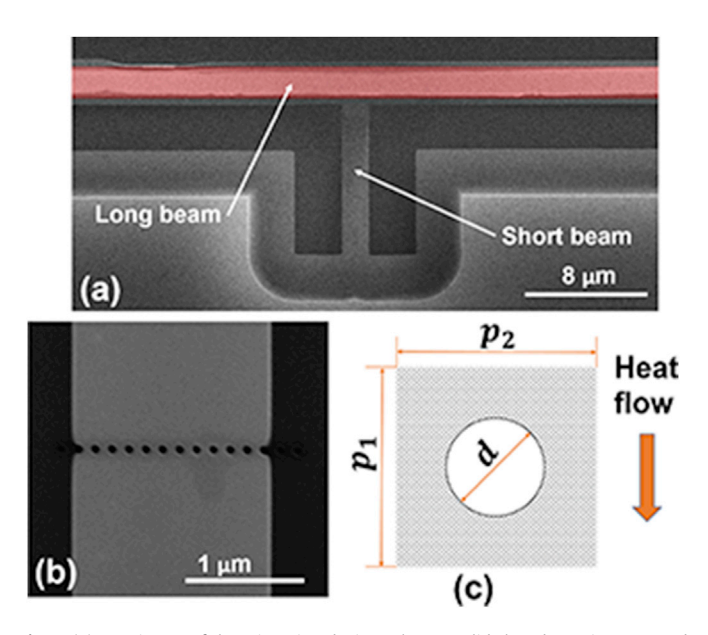


Fig. 1. (a) SEM image of the T-junction device, where a solid short beam is connected to the midpoint of the long beam. The metal-line heater/thermometer along the long beam is highlighted in red color. (b) A typical short beam with one row of nanopores drilled by an FIB. (c) Illustration of key geometric parameters within a period, including d, p_1 , and p_2 .

and ~1.62 μ m wide. It should be noted that uncertainties in the beam width and length should not affect the measured R_{Si} for the nanoporous Si film. In the middle of the measured short beam, periodic nanopores were drilled with an FIB.

The thermal measurements using a T-junction device were based on the steady-state self-heating test of the long beam, where the average temperature rise θ along the long beam can be extracted from the increased electrical resistance of the metal-line heater/thermometer. By comparing θ with and without the short beam, the in-plane thermal resistance of the short beam R_{sh} can be extracted [36,37]. The same T-junction structure has been widely used in previous studies for the thermal measurements of various nanostructures [36-38]. Fig. 1b shows a typical SEM image with one single row of nanopores drilled in the middle of a short beam. In this work, two series of samples with different nanoporous patterns were fabricated and measured. Fig. 1c illustrates a single period of the nanoporous pattern, where d is the pore diameter, and p_1 and p_2 represent the nanopore center-to-center distance along and perpendicular to the heat flow direction, respectively. For two measured samples, the combinations $(d, p_1, \text{ and } p_2)$ are $(70 \pm 5 \text{ nm}, \text{ measured samples})$ 140 ± 15 nm, and 140 ± 5 nm) and $(70 \pm 5$ nm, 270 ± 25 nm, and 250 ± 5 nm), respectively. The larger uncertainty in p_1 is because of the misalignment in sequential FIB drilling. After the first row of nanopores is drilled, one new row of nanopores is added below and above existing nanopores each time. Therefore, the row number of nanopores is N = 0, 1, 3, 5 for measurements of both short beams.

The employed T-iunction microdevice can eliminate the critical sample-device thermal contact resistance. In some earlier studies. the measured thin film was often transferred onto a microdevice consisting of two suspended membranes [9,11,19]. Distortion and possible damage of a sample may easily occur during this transfer process. In addition, the possibly large thermal contact resistance between this thin film and the microdevice was added to the measured thermal resistance of the thin-film sample, leading to a significantly underestimated thermal conductivity *k* of the sample. In some studies, metal or carbon deposition is used to enhance the thermal contact between the sample and the device but unphysical fluctuations in temperature-dependent *k* can often be found due to possibly varied sample-device contacts [9,19]. In this work, the above problems can be eliminated in an integrated device, in which the suspended microdevice and the measured thin film are fabricated from the same Si film. Similar examples can be found elsewhere [26,39-42].

In measurements, continuously adding rows of nanopores to the same short beam eliminated the possible variation between comparison samples fabricated separately. In practice, a series of T-junction devices can be fabricated with electron beam lithography (EBL) patterning and reactive ion etching (RIE), with a different number of nanopore rows in the middle of a short beam. However, the dimension variation between devices will be inevitable, which adds more uncertainties to the comparison between different samples. In this aspect, mask-free FIB drilling on a suspended microdevice is preferred.

All measurements were carried out within a cryostat chamber (Janis VPF-800K) from 85 K to 300 K under a high vacuum ($<1\times10^{-4}$ Torr). A temperature controller (LakeShore 335) was used to maintain a constant temperature for the cold finger, onto which the sample holder was screwed. The sample holder was specially designed to block the radiative heat loss from the sample to the inner wall of the chamber. To measure the thermal resistance of the samples in steady states, a heating dc i_{dc} (up to 500 μ A), coupled with a very weak sensing ac i_{ac} (\sim 3 μ A, \sim 55 Hz), was passed through the metal-line heater. The average temperature rise θ along the long beam was then computed using the electrical resistance rise of the metal line and its calibrated temperature coefficient of

resistance (TCR). This electrical resistance variation was probed with a lock-in amplifier (Stanford Research Systems SR830) to sense the first-harmonic-component voltage signal $V_{ac, 1\omega}$ corresponding to i_{ac} [43]. Temperature-dependent thermal measurements were carried out repeatedly for the same short beam, with nanopore rows added by FIB drilling in the middle of the short beam. After all measurements with the short beam, the short beam was cut with an FIB to carry out the self-heating measurement on the long beam alone, which was used as the baseline in the data analysis. With θ for all measured cases, linear relationships were fitted for i_{ac}^2 and its corresponding θ . The in-plane thermal resistance of the short beam R_{sb} was then extracted by comparing the slopes of the linear fittings for a short beam with varied nanoporous patterns and the slope for the long-beam measurement, as the baseline case.

The length of the short beam (~10 μ m) is specifically designed to accommodate the nanoporous patterns in the middle of the short beam. In general, the nanoporous pattern can dramatically increase the R_{sb} value so that the variation in R_{sb} can be mainly attributed to the thermal resistance of the nanoporous region. To achieve sensitive R_{sb} measurements, a small change in R_{sb} should cause a notable change in θ . In practice, the ratio between thermal resistances of the long and short beams, $\gamma = R_{lb}/R_{sb}$, should be kept in the range 0.0408 < γ < 392 to sense a 20% variation in R_{sb} [36]. Among all measurements, 0.08 < γ < 1.52 is found to satisfy this criterion.

For a bi-layered short beam, the obtained R_{Sb} has the contribution from both Si and SiN_x layers. The thermal resistance of the Si layer (R_{Si}) can be computed as $1/R_{Si}=1/R_{Sb}-1/R_{SN}$, in which R_{SN} is the thermal resistance of the amorphous silicon nitride (SiN_x, or SN) layer. To compute R_{SN} , the employed thermal conductivity k_{SN} for the SiN_x layer was taken from the measurements by Jain and Goodson [44] that used the same deposition temperature (1123 K) as our LPCVD growth. Using either LPCVD or plasma-enhanced chemical vapor deposition, multiple measurements on amorphous SiN_x films with the thickness ranging from 50 nm to 1.5 μ m rendered k_{SN} values of 2.5–4.9 W/m·K at 300 K [44–49]. It was also noted that k_{SN} was not sensitive to the stress [45]. With these k_{SN} values, the thermal conductance $1/R_{SN}$ varied within 4% of the total $1/R_{Sb}$ of a solid film at measured temperatures.

In the data analysis, the employed k_{SN} for a solid SiN_x layer was used to compute the effective thermal resistance R_{SN} of solid or nanoporous SiN_x layers based on the Fourier's law. A commercial software package, COMSOL Multiphysics, was used to calculate R_{SN} for a given temperature and geometry of a porous SiN_x layer. Due to the small heat conduction contribution from the nitride layer, the phonon size effects [50,51] are simply not considered for a nanoporous SiN_x layer. With FIB trimming for the short beam, a 200 ± 20 nm amorphous edge in the Si film can be found on both sides of the short beam, as revealed by TEM studies. The effective width of the short beam is thus reduced to ~1.2 um for the Si laver. Although this effect can be weaker for the amorphous SiN_x layer, the same effective width is simply used for the thermal analysis due to the negligible heat conduction contribution from the SiN_x layer. More discussions for FIB-induced edge defects are given in Section 3. Fig. 2 shows the computed R_{SN} values for a solid SiN_x layer that is 1.2 μm wide, 9.96 μm long, and 34 nm thick, with the error bar indicating the uncertainty due to the dimensions. The R_{SN} value at 85 K is computed with k_{SN} extrapolated from the measurements at 100-300 K.

2.2. Calibration of the short-beam measurements

In calibration, two solid short beams used for the two aforementioned nanoporous patterns have been measured and compared to the measurements of a suspended solid 70-nm-thick

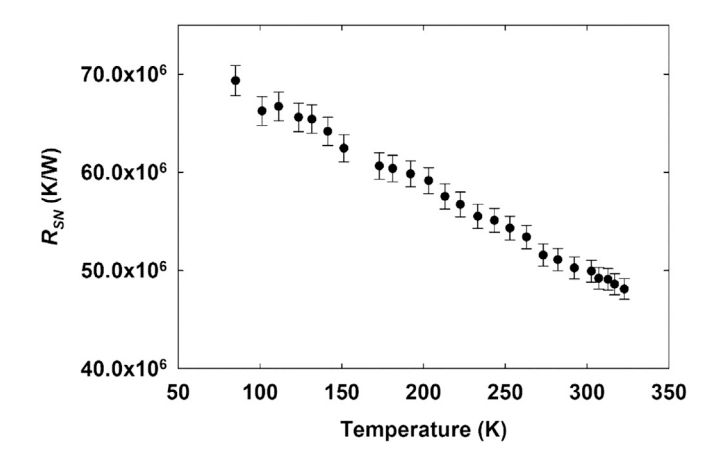


Fig. 2. Thermal resistance R_{SN} of a 34-nm-thick solid SiN_x layer, using k_{SN} given by Ref. [44]. The error bar indicates the uncertainties due to dimensions.

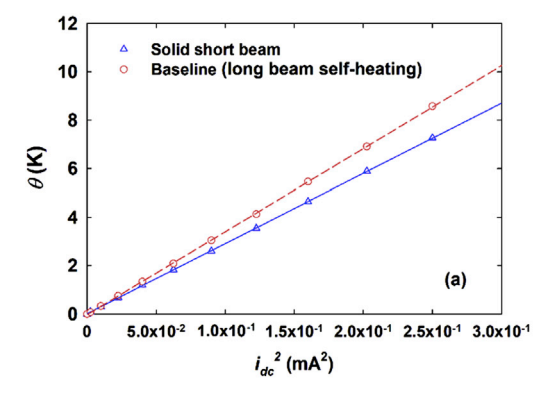
film coated with a metal-film heater and thermometer [21]. Fig. 3a presents the relation between i_{dc}^2 and θ for one sample with a solid short beam and the baseline case, i.e., long beam self-heating without a short beam. A good linearity is found between i_{dc}^2 and θ with the coefficients of determination $R^2 > 0.99994$ for both cases. As anticipated, the y-axis interception of two fitted lines is within 3‰ of the θ range. The thermal conductivity of the solid film can be extracted by comparing the measurements with the short beam and the baseline case without a short beam.

Fig. 3b presents the temperature-dependent thermal conductivities measured for two solid short beams later used for nanoporous patterns, in comparison to the result of a suspended solidfilm bridge with Cr/Pt metal coating [21]. For the T-junction devices, the SiN_x layer contribution was subtracted in the data analysis. Again, an effective short-beam width of 1.2 μm was used for both the Si and SiNx layers. With this modification, the calculated k values for both short beams can agree well with k directly measured from the suspended solid-film bridge that does not have an amorphous edge due to the usage of RIE instead of FIB cutting to pattern the bridge [21]. The uncertainty of R_{sh} for the Tjunction measurements is less than 3% at the 95% confidence interval. For the comparison measurements on a suspended metalcoated solid film, measurements with coupled ac/dc currents and a pure ac current (i.e., 3ω measurements for a suspended sample [52]) agree within 5%, indicating a good accuracy of this comparison measurement. To extract the thermal conductivity of the Si film, the thermal conductance of the metal coating G_{metal} is subtracted from the thermal conductance of the metal-coated Si film. Following the Wiedemann—Franz law, $k \approx k_E = L\sigma T$ and thus $G_{metal} = LT/R$ is expected. Here σ and R are the electrical conductivity and the electrical resistance of the metal coating, respectively. The electrical conductance of the Si film with σ of 5–100 S/m is neglected for its influence on the thermal measurements. The Lorenz number L is obtained from the thermal/electrical measurements of a suspended metal film deposited under the same condition as the metal coating layer. In general, the divergence between the three samples is within 2.2% at all temperatures. At room temperature, the measured $k \approx 59 \text{ W/m} \cdot \text{K}$ is close to the predicted 64 W/m·K for a solid film with the same thickness [53].

2.3. Frequency-dependent phonon Monte Carlo (MC) simulations

When the amorphous edges around adjacent nanopores do not overlap, the nanoporous pattern can be treated as nanopores with an effectively expanded pore diameter. Frequency-dependent phonon MC simulations [27,54] and analytical models [25,27,55,56] can be used to predict the R_{Si} of such a nanoporous Si thin film. In phonon MC simulations, the movement and scattering of particle-like phonons are tracked to statistically obtain the solution for the phonon Boltzmann transport equation (BTE). No wave effects are considered in such simulations. The fitted bulk phonon MFPs for bulk-Si k_I given by Wang et al. [57] are used as the input of the phonon MC simulation. The phonon dispersion is assumed to be isotropic. Only three identical sine-shaped acoustic phonon branches are considered due to the weak thermal conductivity contribution from optical branches [30]. With increased pore-edge phonon scattering along the short beam, R_{Si} obtained by phonon MC simulations is expected to continuously increase with an increased number of nanopore rows. In contrast, coherent phonon transport should lead to saturated R_{Si} when phononic effects are dominant.

The phonon MC simulation is set to be consistent with the experimental setup, where the computed short beam is sandwiched between two black bodies with an applied temperature difference ΔT [58,59]. The exact porous structure can be considered in MC simulations, including the exact pore location and the ~1.2 μ m effective width of the short beam. Both pore edges and top/bottom film surfaces are assumed to diffusively scatter phonons, giving the lower bound of the predicted lattice thermal conductivities. The assumption of diffusive film-surface



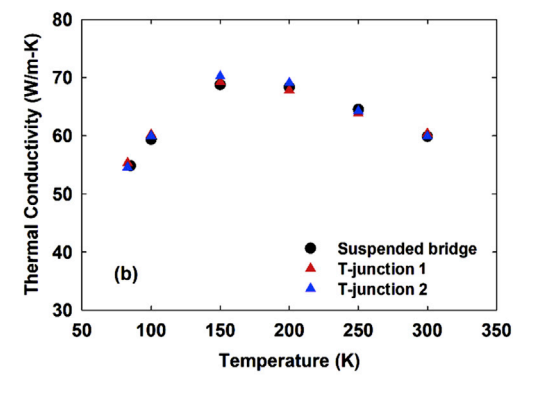


Fig. 3. (a) Measured average temperature rise θ of the long beam as a function of i_{dc}^2 , for cases with a solid short beam and without a solid short beam. The linear fitting is shown as lines. (b) Comparison between T-junction measurements and suspended-bridge measurements of a solid film. For the short beam within the T-junction device, the SiN_x layer contribution is subtracted in the data analysis. For the suspended bridge, the metal-coating contribution to the heat conduction is also subtracted.

phonon scattering is accurate for the measured temperature range of 85–300 K. Above 100 K, molecular dynamics (MD) simulations suggested negligible probability of specular phonon reflection by film surfaces with a roughness as small as 1.63 nm [60]. Experimental studies on the relationship between the surface roughness and the phonon specularity can be found elsewhere [61–63].

Because conventional phonon MC simulations can be extremely expensive for microsized samples, a deviational phonon MC technique [64] is adopted to minimize the computational load. This deviational phonon MC technique only tracks phonons related to the deviation of the phonon distribution function f from the equilibrium distribution function f_0 (i.e., Bose—Einstein distribution) at a reference temperature, leading to orders of magnitude improvement in the computational efficiency [65].

3. Results and discussion

Two aforementioned series of diameter/pitch combinations, namely (70 nm, 140 nm, and 140 nm) and (70 nm, 270 nm, and 250 nm), have been systematically measured with an increased number of nanopore rows on the same short beam. All measurements were carried out from 85 K to 300 K under a high vacuum. For the porous region of these two representative cases, one can be treated as a porous film with an effective pore diameter, whereas the other one can be treated as a highly amorphous film with nanopores.

3.1. Electron microscopy studies

Due to the destructive nature of the FIB, significant pore-edge damage and amorphization are anticipated, including an amorphous surface layer, Ga implantations, lattice defects, and large atom displacement extending tens of nanometers within the collision cascade [66]. Fig. 4a shows the secondary-electrons SEM image of a 70-nm-diameter pore, taken from the SiN_x side. The increased brightness on the pore edge is due to the edge effect for secondary electrons, which results from the tapered pore sidewall by FIB drilling. Such a tapered pore sidewall is highly amorphous, as revealed by previous studies [21]. The nanopores are further examined by energy-dispersive X-ray (EDX) analysis under a TEM. Fig. 4b and c present the element mapping for Si and Ga atoms, respectively. In Fig. 4c, a high concentration of implanted Ga ions can be observed within a pore-edge region of ~40 nm width. A reduced concentration of Ga ions can be found even beyond this region. A largely reduced thermal conductivity is expected for this highly amorphous region. When a much higher current (20 nA vs 77 pA for pore drilling) and the same voltage (30 keV) are used for the FIB cutting of the long and short beams, this amorphous edge region can be as wide as ~200 nm in estimation. In physics, coherent phonon phase and the corresponding wave effect can be largely destroyed due to phonon scattering by amorphous pore edges. With further reduced nanopore spacing, the amorphous region can largely overlap (Fig. 4d), leading to a completely amorphous region with nanopores.

Fig. 5a shows an illustration of a pore with amorphous pore edges. The SEM images of the same short beam with one, three, and five rows of nanopores are shown in Fig. 5b—d. The leftmost and rightmost columns of nanopores in Fig. 5b—d already lie within the amorphous edge on both sides of the short beam, leading to negligible influence on the R_{Si} value of the whole short beam. Based on TEM studies, the effective pore diameter d_{eff} is estimated to be ~160 nm.

3.2. Pattern with an effectively expanded pore diameter

For the (70 nm, 270 nm, and 250 nm) patterns, an effective $d_{eff} = 160$ nm can be assigned to nanopores to match the predictions by frequency-dependent phonon MC simulations with the experimental results. This $d_{\it eff}$ value is consistent with the estimation by microscopy studies. Fig. 6 presents measured R_{Si} (symbols) as a function of the row number N for nanopores. With nanopores to affect the thermal transport, R_{Si} is significantly increased from the thermal resistance of a solid short beam, i.e., 1.72×10^6 to 2.16×10^6 K/W at 85–300 K. For N>1, linear correlations between N and R_{Si} can be found at all measured temperatures, indicating strong incoherent phonon transport. The $N-R_{Si}$ slope for $N \ge 1$ is different from the slope from N = 0 points to N = 1 points, which can be attributed to the large change in the heat flow pattern after adding one row of nanopores. The error bar is for the uncertainty at the 95% confidence interval. In general, the relative error becomes larger for increased N because the contrast between measurements with and without the short beam is decreased for a high R_{Si} . Along another line, the measurements generally agree with the predictions by phonon MC simulations (lines). When incoherent phonon transport is dominant, then up to 25 nm displacement of FIB-drilled nanopores has negligible influence on R_{Si} , which is evident in the unchanged radiative MBL of the nanoporous pattern. In existing experiments, the periodic and aperiodic patterns should render the same thermal conductivity without any wave effects [5,26,67]. Our results contradict with an earlier study on FIB-drilled nanoporous films with minimum feature sizes >100 nm. which suggests coherent phonon transport at 300 K [11].

The increase in R_{Si} with added nanopores is anticipated as the result of increased phonon boundary scattering by pore edges within the volume. In previous studies, the scattering cross-section of nanopores per unit volume [68] or simply the volumetric interface/surface area [69,70] were recognized as the key parameter for the k_I reduction in a particle-in-a-host nanocomposite or nanoporous materials as the special case with zero-thermalconductivity nanoparticles. For nanoporous materials, it was later pointed out by Machrafi and Lebon [71] that the solid volume instead of the total volume should be used in the calculations of the volumetric pore surface area. The obtained volumetric pore surface area was simply associated with the MBL as the characteristic length of the nanoporous structure [2,27,28]. For the measured short beam with an extremely low porosity, the reciprocal of the MBL simply linearly increases with added nanopore rows. When incoherent phonon transport is dominant, the reduced MBL should lead to continuously increased R_{Si} with increased N, as observed here. In contrast, the measured R_{Si} should saturate when coherent phonon transport becomes critical.

3.3. Pattern with a completely amorphous porous region

For the (70 nm, 140 nm, and 140 nm) pattern, the highly overlapped amorphous pore-edge region leads to a completely amorphous film with nanopores (Fig. 7a). The central part of the amorphous region has more Ga implantation due to multiple exposure under the FIB cutting. In this amorphous region, the thermal transport is partially contributed by non-propagating "diffusive" modes or diffusons, as suggested by MD simulations on nanoporous Si films [72,73] or Si nanowires with amorphous surfaces [74]. In practice, the thermal conductivity of a Si thin film can be reduced by depositing Al, resulting from the formed interface with intermixed Al and Si atoms [75,76]. Within amorphous materials, heat can also be transported by propagating vibrational modes as "propagons" [77—79]. Related studies on thermal transport within nanoporous and amorphous SiN_x films are available [50,51].

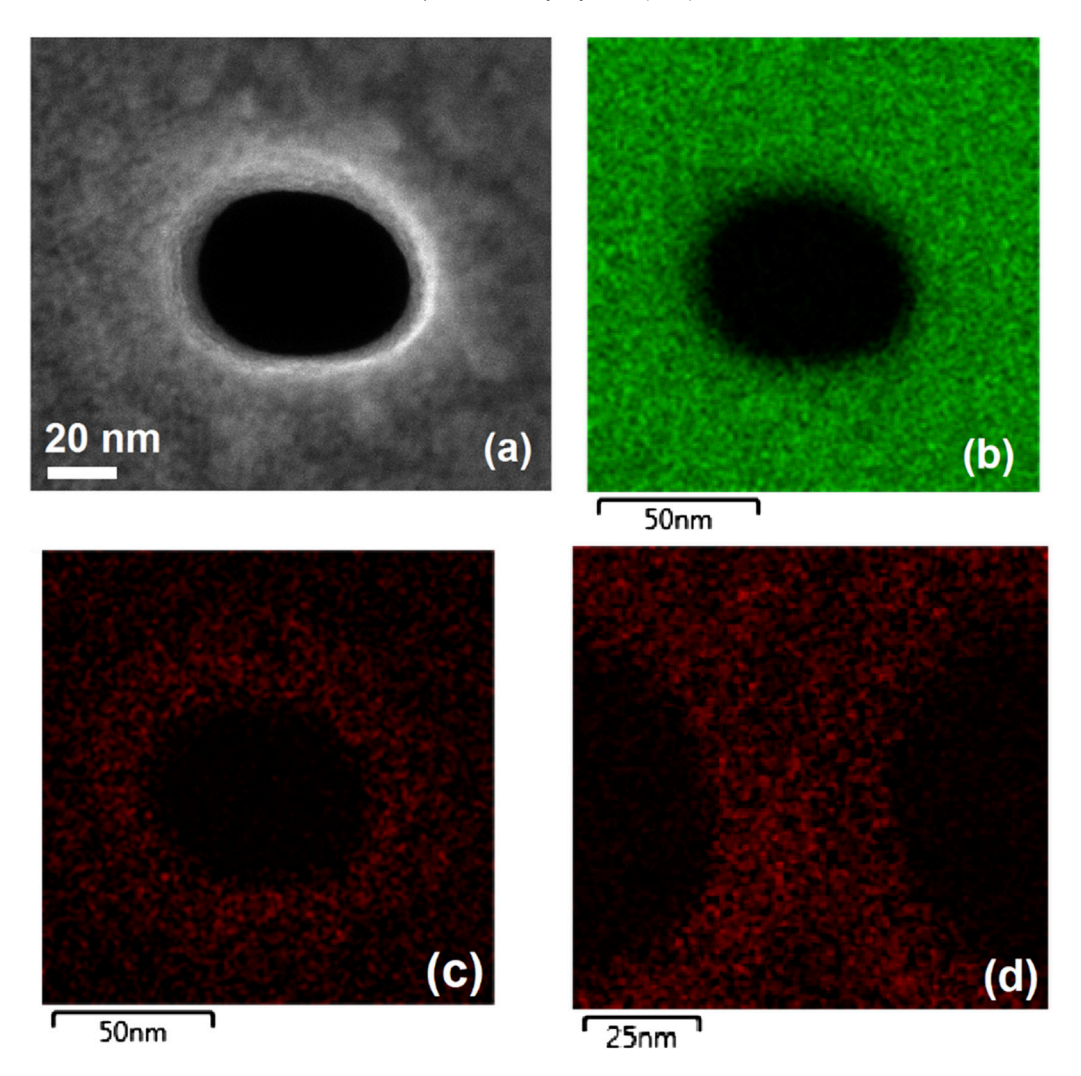


Fig. 4. (a) SEM image of the region around a 70-nm-diameter pore, taken from the SiN_x side. Element mapping of (b) Si and (c) Ga around a nanopore. (d) Largely overlapped amorphous nanopores region with ~50 nm neck width, shown by Ga element mapping.

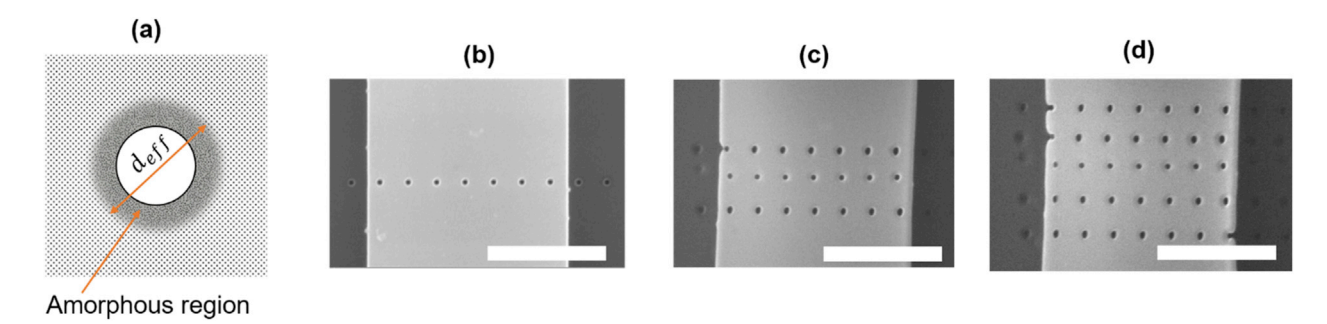


Fig. 5. (a) Concept of a nanopore with an effectively expanded pore diameter *d_{eff}* due to pore-edge amorphization. (b–d) SEM images of the same short beam drilled with (b) one, (c) three, and (d) five rows of nanopores for the (70 nm, 270 nm, and 250 nm) sample. Scale bar is 1 μm for the three SEM images.

In measurements, R_{Si} values do not saturate with an increased N (Fig. 7b). The temperature dependence of R_{Si} is further displayed in Fig. 7c. For a given N value, the largest R_{Si} within the measured temperature range is found at 85 K. For amorphous materials, $k \approx k_L$ within the measured temperature range usually follows the trend of the specific heat [80–82]. In this case, k generally increases at elevated temperatures, leading to a decreased R_{Si} at a higher temperature. In contrast, a nanoporous crystalline Si film often reaches

its peak k at a cryogenic temperature when the phonon MFPs are still restricted by the characteristic length such as the MBL [21]. Above this temperature, k starts to decrease due to enhanced internal phonon scattering to further decrease the phonon MFPs below the characteristic length. In this case, the smallest k for the nanoporous region and thus the largest $R_{\rm Si}$ may occur at 300 K, as shown in Fig. 6.

In general, the (70 nm, 140 nm, and 140 nm) pattern has a much higher $R_{\rm Si}$ than the (70 nm, 270 nm, and 250 nm) pattern. The

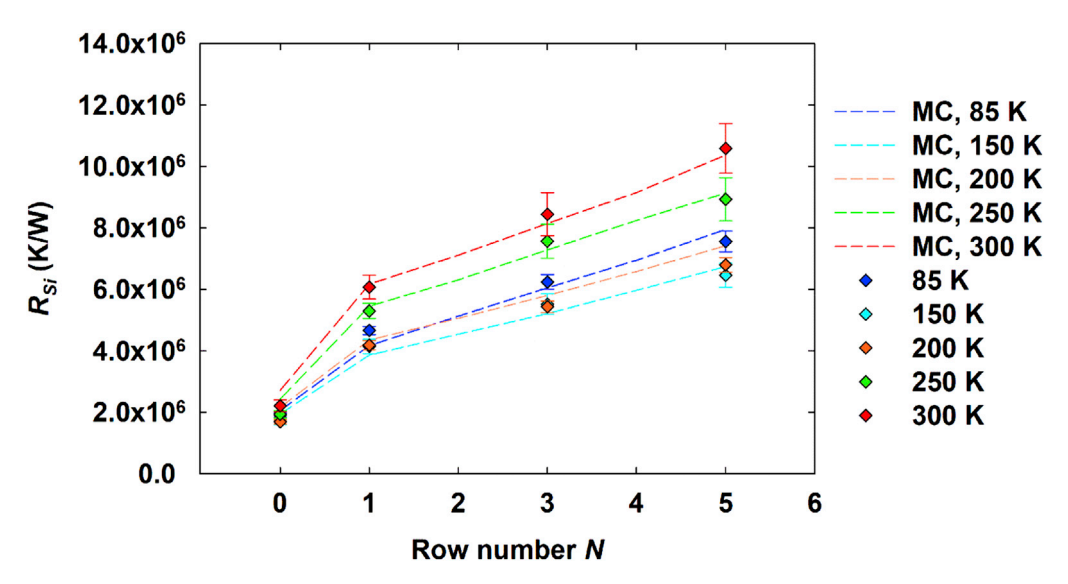


Fig. 6. The thermal resistance R_{Si} of the nanoporous Si layer as a function of the row number N for the (70 nm, 270 nm, and 250 nm) pattern. The error bar indicates the 95% confidence interval. The almost linear relationship between R_{Si} and $N \ge 1$ suggests strong incoherent phonon transport.

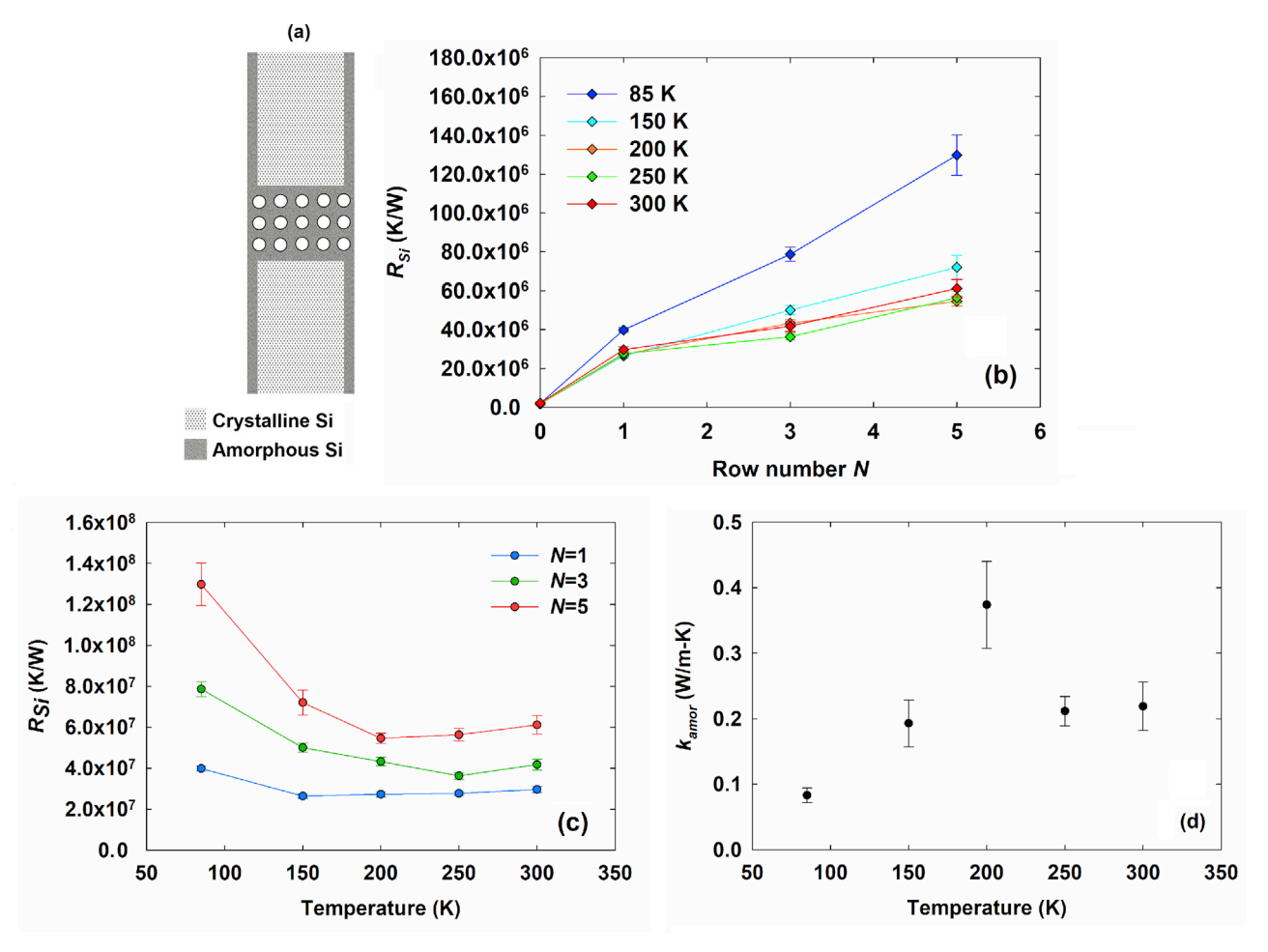


Fig. 7. (a) Schematic drawing of a short beam with a highly amorphous porous region. (b) Measured R_{Si} as a function of the row number for the (70 nm, 140 nm, and 140 nm) pattern. (c) Temperature-dependent R_{Si} . (d) Temperature-dependent k_{amor} in estimation. All error bars are for the 95% confidence interval.

conventional Fourier law is reasonably accurate for this amorphous region mainly with diffusons. The existence of such propagons leads to some size-dependent k_L in nanoporous patterns. Nevertheless, the solid k value of the amorphous region (k_{amor}) can be estimated from the change of R_{Si} for increased N values. Within the measuring temperature range, k_{amor} is estimated to be less than 0.4 W/m·K, using R_{si} difference between row number N=3 and N = 5, and pattern dimensions including the pitch, effective short beam width, and film thickness.

The temperature-dependent estimated k_{amor} is presented in Fig. 7d. The higher k_{amor} at 200 K does not follow the trend of other points, which may be attributed to the uncertainties in its estimation. Nevertheless, the estimated k_{amor} is lower than $k \sim 1 \text{ W}/$ m·K as the amorphous limit for Si at 300 K [83]. The low k_{amor} can be attributed to the implanted heavy Ga ions across the nanoporous region, which may dramatically reduce the lattice vibration frequencies and thus the thermal conductivity. For general materials, doping heavy atoms to the material (i.e., increased mean atomic mass) has been widely used to reduce the k [84–86]. For Al₂O₃, only 0.1% Nd dopant density can reduce the velocity of transverse phonons by ~600 m/s, indicating a profound impact on the lattice vibration modes and thus the k [86]. Comparing with $k \approx 59 \text{ W/m} \cdot \text{K}$ for the starting solid film, such an extremely low k_{amor} value supports the simplification of neglecting the amorphous edges on both sides of the short beam in the data analysis.

4. Conclusion

In this work, the possible impact of phonon coherence within FIB-drilled nanoporous Si films is evaluated by comparing the thermal resistance R_{Si} of the same Si short beam with increased rows of nanopores. The almost linearly increased R_{Si} as a function of the row number $N \ge 1$ indicates negligible coherent phonon transport. Special attention should also be paid to the pore-edge defects induced by an FIB. Contrast can be found between nanoporous patterns with the neck width wider or narrower than the amorphous-edge region between adjacent nanopores. Particularly for a highly amorphous nanoporous region created by FIB drilling, the solid thermal conductivity is found to be much lower than k~1 W/m·K as the amorphous limit for Si. The dramatically reduced thermal conductivity due to FIB-introduced pore-edge defects can be widely used for on-chip thermal management of thin-filmbased electronic devices and thermal waveguide [5,87,88].

Although the samples measured in this work do not have notable phononic effects, the demonstrated approach can always be used when strong phononic effects exist within periodic nanoporous thin films or 2D materials. In this situation, the short-beam thermal resistance is anticipated to saturate with added rows of nanopores. At 300 K, strong phononic effects require ultrafine patterns with a sub-10 nm periodic length that is comparable to the phonon wavelength, e.g., 1–10 nm for bulk Si at room temperature [15,16]. Smooth pore edges are also necessary to minimize the diffusive pore-edge phonon scattering that destroys phononic effects. Considering the challenges in fabricating such ultrafine and high-quality nanoporous patterns, it is easier to achieve phononic effects at the cryogenic temperature, where the dominant phonon wavelength becomes much longer than that at room temperature.

Credit author statement

Q. Hao conceived the whole experiments and wrote the initial draft. Y. Xiao carried out all data analysis and simulations; Xiao also helped to finalize part of the paper. D. C. Xu carried out the nanofabrication and the thermal measurements. F. J. Medina helped for the electron microscopy studies. S. E. Wang helped for the data analysis.

Declaration of interests

The authors declare that they have no known competing financial interests or personal relationships that could have appeared to influence the work reported in this paper.

Acknowledgments

FIB characterizations and TEM and SEM analyses were performed at the Kuiper Materials Imaging and Characterization Facility and the authors gratefully acknowledge NASA (grant numbers NNX12AL47G and NNX15AJ22G) and NSF (grant number 1531243) for funding of the instrumentation in the Kuiper Materials Imaging and Characterization Facility at the University of Arizona. The authors also thank TEM manager Jerry Chang for his assistance. The authors thank the University of Arizona Research Computing High Performance Computing (HPC) and High Throughput Computing (HTC) for the allocation of computing time. This work supported by the U.S. Air Force Office of Scientific Research (grant number FA9550-16-1-0025) for studies of nanoporous structures and the National Science Foundation (grant number CBET-1651840) for studies on phonon MC simulations. The authors also acknowledge resources and support from the NanoFab facility, part of the Knowledge Enterprise Core Research Facilities at Arizona State University.

References

- [1] D.G. Cahill, et al., Appl. Phys. Rev. 1 (1) (2014): 011305.
- [2] Y. Xiao, et al., ES Mater. Manuf. 5 (2019) 2.
- A.M. Marconnet, et al., J. Heat Tran. 135 (6) (2013): 061601.
- M. Nomura, et al., Jpn. J. Appl. Phys. 57 (8) (2018): 080101.
- R. Anufriev, et al., Nat. Commun. 8 (2017) 15505.
- [6] M. Maldovan, Phys. Rev. Lett. 110 (2) (2013): 025902.
- M. Maldovan, Nature 503 (2013) 209.
- E. Dechaumphai, R. Chen, J. Appl. Phys. 111 (7) (2012): 073508.
- J.-K. Yu, et al., Nat. Nanotechnol. 5 (10) (2010) 718.
- [10] P.E. Hopkins, et al., Nano Lett. 11 (1) (2010) 107. S. Alaie, et al., Nat. Commun. 6 (2015) 7228.
- [12] P.E. Hopkins, et al., Appl. Phys. A 103 (3) (2011) 575.
- Y. Gong, et al., Optic Express 18 (3) (2010) 2601. [13]
- [14] M. Makarova, et al., Appl. Phys. Lett. 89 (22) (2006) 221101.
- [15] K. Esfarjani, et al., Phys. Rev. B 84 (8) (2011): 085204.
- [16] A. Jain, et al., Phys. Rev. B 87 (19) (2013) 195301.
- [17] A.M. Marconnet, et al., Nanoscale Microscale Thermophys. Eng. 16 (4) (2012)
- [18] M.R. Wagner, et al., Nano Lett. 16 (9) (2016) 5661.
- [19] J. Tang, et al., Nano Lett. 10 (10) (2010) 4279.
- [20] N.K. Ravichandran, A.J. Minnich, Phys. Rev. B 89 (20) (2014) 205432.
- [21] Q. Hao, et al., Sci. Rep. 8 (1) (2018) 9056.
- H. Machrafi, et al., Int. J. Heat Mass Tran. 97 (2016) 603.
- M. Criado-Sancho, et al., Phys. Lett. 376 (19) (2012) 1641.
- [24] H. Machrafi, Appl. Math. Model. 40 (3) (2016) 2143.
- [25] L. Zhang, G. Ouyang, J. Phys. Appl. Phys. 51 (34) (2018) 345303. I. Lee, et al., Nat. Commun. 8 (2017) 14054. [26]
- Q. Hao, et al., J. Appl. Phys. 120 (6) (2016): 065101.
- [28] Q. Hao, et al., Appl. Therm. Eng. 111 (2017) 1409.
- [29] H.C. Hottel, W.H. McAdams, Heat Transmission, 1954.
- G. Chen, Nanoscale Energy Transport and Conversion: A Parallel Treatment of Electrons, Molecules, Phonons, and Photons, Oxford University Press, New York, 2005.
- [31] B. Graczykowski, et al., Phys. Rev. B 91 (7) (2015): 075414.
- D. Xu, et al., Carbon 144 (2019) 601.
- T.G. Pedersen, et al., Phys. Rev. Lett. 100 (13) (2008) 136804. [33]
- [34] L. Hu, et al., J. Heat Tran. 126 (5) (2004) 786.
- [35] M.N. Luckyanova, et al., Science 338 (6109) (2012) 936.
- [36] C. Dames, et al., Rev. Sci. Instrum. 78 (10) (2007) 104903.
- M. Fujii, et al., Phys. Rev. Lett. 95 (6) (2005): 065502.
- [38] W. Jang, et al., Appl. Phys. Lett. 103 (13) (2013) 133102.
- W. Park, et al., Nanoscale 10 (23) (2018) 11117.
- [40] B. Kim, et al., Thermal conductivity manipulation in single crystal silicon via lithographycally defined phononic crystals, in: Micro Electro Mechanical Systems (MEMS), 2012 IEEE 25th International Conference on, IEEE, 2012,
- [41] D. Song, G. Chen, Appl. Phys. Lett. 84 (5) (2004) 687.
- [42] J. Lim, et al., ACS Nano 10 (1) (2016) 124.

- [43] L. Shi, et al., J. Heat Tran. 125 (2003) 881.
- [44] A. Jain, K.E. Goodson, J. Heat Tran. (10) (2008) 130.
- [45] H. Ftouni, et al., Phys. Rev. B 92 (12) (2015) 125439.
- [46] A. Sikora, et al., Rev. Sci. Instrum. 83 (5) (2012): 054902.
- [47] A. Sikora, et al., Rev. Sci. Instrum. 84 (2) (2013): 029901.
- [48] M.C. Wingert, et al., Semicond. Sci. Technol. 31 (11) (2016) 113003.
- [49] D.R. Queen, F. Hellman, Rev. Sci. Instrum. 80 (6) (2009): 063901.
- [50] N. Tambo, et al., QN04.12.02 : suppression of propagon heat transport in amorphous silicon nitride phononic crystals, in: 2019 MRS Spring Meeting and Exhibit, 2019., Phoenix, Arizona, USA.
- Y. Liao, et al., ON04.12.04: thermal transport in amorphous phononic crystals. in: 2019 MRS Spring Meeting and Exhibit, 2019. Phoenix, Arizona, USA.
- [52] L. Lu, et al., Rev. Sci. Instrum. 72 (7) (2001) 2996.
- [53] C. Jeong, et al., J. Appl. Phys. 111 (9) (2012): 093708.
- [54] Q. Hao, et al., J. Appl. Phys. 116 (11) (2009), 114321/1.
 [55] Y.-C. Hua, B.-Y. Cao, J. Phys. Chem. C 121 (9) (2017) 5293.
- [56] C. Huang, et al., Phys. E Low-dimens. Syst. Nanostruct. 97 (2018) 277.
 [57] Z. Wang, et al., Nano Lett. 11 (6) (2011) 2206.
- [58] Q. Hao, et al., J. Appl. Phys. 106 (11) (2009) 114321.
- [59] S. Mazumder, A. Majumdar, J. Heat Tran. 123 (4) (2001) 749.
- [60] X. Wang, B. Huang, Sci. Rep. 4 (2014) 6399.[61] N.K. Ravichandran, et al., Phys. Rev. X 8 (4) (2018): 041004.
- [62] D. Gelda, et al., Phys. Rev. B 97 (4) (2018): 045429.
- [63] LS. Heron, et al., Nano Lett. 9 (5) (2009) 1861.
- [64] J.-P.M. Péraud, N.G. Hadjiconstantinou, Phys. Rev. B 84 (20) (2011) 205331.

- [65] T. Luo, G. Chen, Phys. Chem. Chem. Phys. 15 (10) (2013) 3389.
- [66] L.A. Giannuzzi, F.A. Stevie, Micron 30 (3) (1999) 197.
- [67] B. Graczykowski, et al., Nat. Commun. 8 (1) (2017) 415.
- [68] M. Kashiwagi, et al., Physical Review Applied 10 (4) (2018): 044018.
- [69] A. Minnich, G. Chen, Appl. Phys. Lett. 91 (7) (2007): 073105.
- [70] M.-S. Jeng, et al., J. Heat Tran. 130 (4) (2008): 042410.
- [71] H. Machrafi, G. Lebon, Phys. Lett. 379 (12–13) (2015) 968.
 [72] V.L. Deringer, et al., J. Phys. Chem. Lett. 9 (11) (2018) 2879.
- [73] Y. He, et al., ACS Nano 5 (3) (2011) 1839.
- [74] D. Donadio, G. Galli, Phys. Rev. Lett. 102 (19) (2009) 195901.
- [75] R. Anufriev, et al., Nanoscale 9 (39) (2017) 15083.
- [76] A. George, et al., ACS Appl. Mater. Interfaces 11 (12) (2019) 12027.
- [77] J. Moon, et al., Phys. Rev. B 97 (2) (2018): 024201. [78] S. Kwon, et al., ACS Nano 11 (3) (2017) 2470.
- [79] J.M. Larkin, A.J.H. McGaughey, Phys. Rev. B 89 (14) (2014) 144303.
 [80] A. Einstein, Ann. Phys. 35 (1911) 679.
- [81] D.G. Cahill, R.O. Pohl, Solid State Commun. 70 (10) (1989) 927.
- [82] B.L. Zink, et al., Phys. Rev. Lett. 96 (5) (2006): 055902.
- [83] D.G. Cahill, et al., Phys. Rev. B 46 (10) (1992) 6131.
 [84] M.R. Winter, D.R. Clarke, J. Am. Ceram. Soc. 90 (2) (2007) 533.
- [85] Y. Pei, et al., Adv. Mater. 24 (46) (2012) 6125. [86] F. Kargar, et al., Appl. Phys. Lett. 112 (19) (2018) 191902.
- [87] Y. Zeng, A. Marconnet, Physical Review Applied 9 (1) (2018): 011001.
- [88] G. Romano, J.C. Grossman, Appl. Phys. Lett. 105 (3) (2014): 033116.